# A method for atlas-based volumetric registration with surface constraints for Optical Bioluminescence Tomography in small animal imaging

Abhijit J. Chaudhari, Anand A. Joshi, Felix Darvas and Richard M. Leahy

*Signal and Image Processing Institute, University of Southern California,*
*Los Angeles, CA 90089, USA*

## ABSTRACT

Atlases are normalized representations of anatomy that can provide a standard coordinate system for in vivo imaging studies. For Optical Bioluminescence Tomography (OBT) in small animals, the animal's surface topography can be reconstructed from structured light measurements, but internal anatomy is unavailable unless additional CT or MR images are acquired. We present a novel method for estimating the internal organ structure of a mouse by warping a labeled 3D volumetric mouse atlas with the constraint that the surfaces of the two should match. Surface-constrained harmonic maps used for this bijective warping are computed by minimizing the covariant harmonic energy. We demonstrate the application of this warping scheme in OBT, where scattering and absorption coefficients of tissue are functions of the internal anatomy and hence, better estimates of the organ structures can lead to a more accurate forward model resulting in improved source localization. We first estimated the subject's internal geometry using the atlas-based warping scheme. Then the mouse was tessellated and optical properties were assigned based on the estimated organ structure. Bioluminescent sources were simulated, an optical forward model was computed using a finite-element solver, and multispectral data were simulated. We evaluate the accuracy of the forward model computed using the warped atlas against that assuming a homogeneous mouse model. This is done by comparing each model against a 'true' optical forward model where the anatomy of the mouse is assumed known. We also evaluate the impact of anatomical alignment on bioluminescence source localization.

**Keywords:** Volumetric Registration, Optical Bioluminescence Tomography, Atlas-based methods.

## 1. INTRODUCTION

Anatomical atlases are useful tools for molecular studies involving modalities that do not image anatomical structure, e.g. Positron Emission Tomography (PET) and Optical Bioluminescence Tomography (OBT).[1] Functional images can be overlaid on the atlas for visualization and quantitation with respect the underyling anatomy. For OBT in small animals, where the objective is to estimate the 3D distribution of a bioluminescent source in the animal volume from optical signal measurements on the animal surface, knowledge of internal organ geometry is also important for the accurate modeling of light propagation through tissue.[2,3] This is because the optical properties of tissue, such as the reduced scattering coefficient $\mu'_s$ and the absorption coefficient $\mu_a$, vary in different tissue types, and misalignment of internal organs may lead to source localization errors.[4]

Before it can be used for these purposes, the atlas must first be aligned with the anatomy of the individual animal being studied. Unfortunately, anatomical information is generally not available in an optical system unless CT or MRI images are also acquired.[5] However, limited anatomical information in the form of the mouse surface topography can be estimated by projecting a structured light pattern onto the animal and using a phase unwrapping algorithm.[6] Here we explore the use of a mouse atlas (e.g. the Digimouse[1]) for which the anatomy and optical properties are well defined. This atlas is warped to match the shape of the individual mouse using surface constraints. We note that deformable atlases have been previously used for estimating internal anatomy in OBT studies. However, the registration procedure in that case was carried out using a CT image of the mouse being studied.[7]

Rigid and nonrigid registration approaches performing volumetric warping can use landmark points, curves and surfaces as additional constraints in combination with intensity-based matching.[8–14] These methods combine landmarks, curves[14] and image matching[13] in a large deformations framework ensuring generation of diffeomorphisms.[15–17] Registration methods such as HAMMER[18] incorporate geometric as well as intensity information for alignment. In contrast, nonrigid alignment of volumes in the absence of internal intensity values and based on only surface information is a more ill-posed problem due to the potential for anatomical variability within the subject. Our goal in this paper is to investigate whether such a procedure can lead to useful alignment of the atlas, producing improvements in the forward model for OBT compared to the standard homogeneous assumption. We use a harmonic mapping based method to perform volumetric registration between the atlas and a subject mouse based only on the animal shape. The warping transformation is then applied to the atlas to produce an estimate of the internal anatomy of the subject.

The variation with wavelengths in the optical properties of different tissues can be used to reduce the ill-posedness of the OBT inverse problem.[3, 19] Consequently, the use of multispectral data for image reconstruction tends to yield better deep source reconstruction results compared to those obtained using achromatic or monochromatic data. Commercial systems are available (e.g. Xenogen Corporation's IVIS 200) that use passive wavelength filters for multispectral data collection. Furthermore, mirror systems like the one described in[3] can be used in conjunction with commercially available systems for tomographic optical data collection. For this study, we simulate multispectral tomographic data similar to that generated using the mirror setup and the IVIS 200 described by Chaudhari et al.[3]

In this paper we first describe the surface and volumetric registration method using harmonic maps for registering two mouse volumes. We also describe a procedure for generating the multispectral OBT forward model using the organ boundaries generated by the warping scheme described here. We show comparisons between the volumetric registration approach presented here and a rigid registration method.[20] This is done by computing dice coefficients that are indicators of organ overlap.[21] Further, we compare optical reconstruction results for representative sources placed in the kidneys, stomach, lungs, heart and brain using our atlas-based inhomogeneous forward model in comparison to a homogeneous forward model.

## 2. SURFACE AND VOLUME ALIGNMENT

We assume that the surface of the mouse being studied is available. The registration of the Digimouse atlas to the subject is done in two steps. First we align the two surfaces, i.e. we define a one to one mapping between the two surfaces. We then compute a volumetric map between the two volumes while retaining the surface correspondence.

### 2.1. Surface Alignment

As an initialization for the volumetric registration procedure described next, the surfaces of the two mouse volumes need to be aligned. To do this we use the intrinsic thin-plate spline based surface registration method described by Joshi et al.,[22] which produces a bijective point correspondence between the two mouse surfaces by aligning 2D coordinate systems defined on both surfaces. This is achieved by first mapping each of the two surfaces to two unit squares, each square representing one half of the mouse surface, with the boundary corresponding to the midsagital plane. We then align surface landmarks by computing a coordinate deformation field that aligns the landmark coordinates. The deformation is regularized using the thin-plate bending energy computed with respect to the intrinsic geometry of the surfaces using a covariant bi-harmonic equation. We refer the reader to Joshi et al.[22] for a detailed description of this method. Landmarks on the surface must be defined by the user and in the examples shown later included curves drawn along each limb.

### 2.2. Volume Alignment

The surface registration procedure sets up a point to point correspondence between the subject and the template mouse surfaces. We then need to extrapolate this correspondence from the surface of the mice to the entire volume to produce a one-to-one map. 3D harmonic maps are attractive for this purpose due to their tendency to be bijective if the boundaries (surfaces) are mapped bijectively.

Given two 3D manifolds $M$ and $N$ representing mouse volumes, with boundaries $\partial M$ and $\partial N$ representing the corresponding surfaces, we want to find a map from $M$ to $N$ such that $\partial M$, the surface of $M$, maps to $\partial N$, the surface of $N$. Let $u : M \rightarrow N$ be a $C^\infty$ map from a 3D Riemannian manifold $(M, g)$ to a 3D Riemannian manifold $(N, h)$ where $g$ and $h$ are Riemannian metrics for $M$ and $N$ respectively. Let $(x^1, x^2, x^3)$ and $(y^1, y^2, y^3)$ be local coordinates for $x$ and $u(x)$ respectively. The *mapping energy* in coordinate form[23] is given by:

$$E(u) = \frac{1}{2} \int_M \sum_{i,j=1}^3 \sum_{\alpha,\beta=1}^3 g^{ij}(x) h_{\alpha\beta}(u(x)) \frac{\partial u^\alpha(x)}{\partial x^i} \frac{\partial u^\beta(x)}{\partial x^j} d\mu_g, \tag{1}$$

where the integration is over the manifold $M$ with respect to the intrinsic measure $d\mu_g$ induced by its Riemannian metric $g$. A *harmonic map* from $(M, g)$ to $(N, h)$ is defined to be a critical point of the mapping energy $E(u)$.

To compute an optimal mapping for the surface as well as the interior, we allow the surface $M$ to flow within the surface of $N$ when computing the map. The only constraints placed on the surfaces are that the maps are aligned at a set of user defined landmarks. This less restrictive surface mapping constraint cannot be formulated directly in the ambient Euclidean 3D space since there is no analytical expression for the surfaces, although this could be accomplished without parameterizing the surface using a level set approach.[24, 25] Here we use an intermediate representation for the manifolds which allows us to enforce the boundary matching constraint while allowing one boundary to flow within the other. This is achieved by first mapping the subject volume to the unit ball.

We find the map $v$ from the manifold $N$ to the unit ball $B(0, 1)$ using a method described in Wang et al.[26] (Figure 1). This map is bijective and therefore we can treat the unit ball $B(0, 1)$ as an alternative representation $(N, h)$ of the manifold $N$, with associated metric $h$. It has an advantage over the Euclidean space $(N, I)$ that the surface $\partial N$ lies on the sphere ($I$ represents the identity metric for the Euclidean space). Now instead of needing to directly compute the harmonic map $u : (M, I) \rightarrow (N, I)$, we instead find the harmonic map $\tilde{u} : (M, I) \rightarrow (N, h) \approx B(0, 1)$ subject to the constraint that the surface $\partial M$ maps to the spherical boundary of the unit ball, as illustrated in Figure 1. The final harmonic mapping from $u : (M, I) \rightarrow (N, I)$ can then be computed as $u = v^{-1} \circ \tilde{u}$ as illustrated in Figure 1 (a).

The harmonic mapping problem now becomes:

$$\tilde{u} = \arg \min_\gamma \int_M \sum_{i=1}^3 \sum_{\alpha,\beta=1}^3 h_{\alpha\beta}(\gamma(x)) \left( \frac{\partial \gamma^\alpha(x)}{\partial x^i} \right) \left( \frac{\partial \gamma^\beta(x)}{\partial x^i} \right) d\mu_g \tag{2}$$

subject to $\|\tilde{u}\|^2 = 1$ for $s \in \partial M$, the surface of $M$. Note that this constraint allows the surface map to flow within the spherical boundary.

### 2.2.1. Initialization Procedure

Because the minimization problem is nonlinear, it is important to have a good initial estimate of the map $\tilde{u}$ in order to achieve convergence in a reasonable amount of time. We therefore generate an initial estimate $\tilde{u}_0$ of $\tilde{u}$ by also computing a map of the second manifold $(M, I)$ to the unit ball, just as we do for the first manifold $(N, I)$ (Figure 1 (b)). To compute mappings of mouse volumes to the unit ball, we first compute a mapping of the surfaces to the unit sphere with curve landmark alignment as described in Section 2.1. The interior of each manifold is mapped to the unit ball by computing volumetric harmonic maps. Thus, our initialization method generates a bijective initial map, which is not necessarily harmonic, by first aligning two surfaces using the surface matching process. Using these surface maps as constraints, we then map $M$ and $N$ to the unit ball to provide, respectively, the manifold $(N, h)$ and an initial estimate $\tilde{u}_0$ of the desired map $\tilde{u}$ from $(M, I)$ to $(N, h)$. The initial map obtained in this manner is smooth and bijective. With this initialization, we then compute the 3D harmonic map by minimizing (2) to obtain the desired harmonic map. The initialization procedure is illustrated in Figure 1 (b).

We now describe the procedures by which we produce harmonic maps from $M$ and $N$ to the unit ball, and the subsequent refinement of $\tilde{u}_0$ to $\tilde{u}$ that minimizes the harmonic energy of the map from $M$ to $N$. In the

(a) Schematic             (b) Initialization
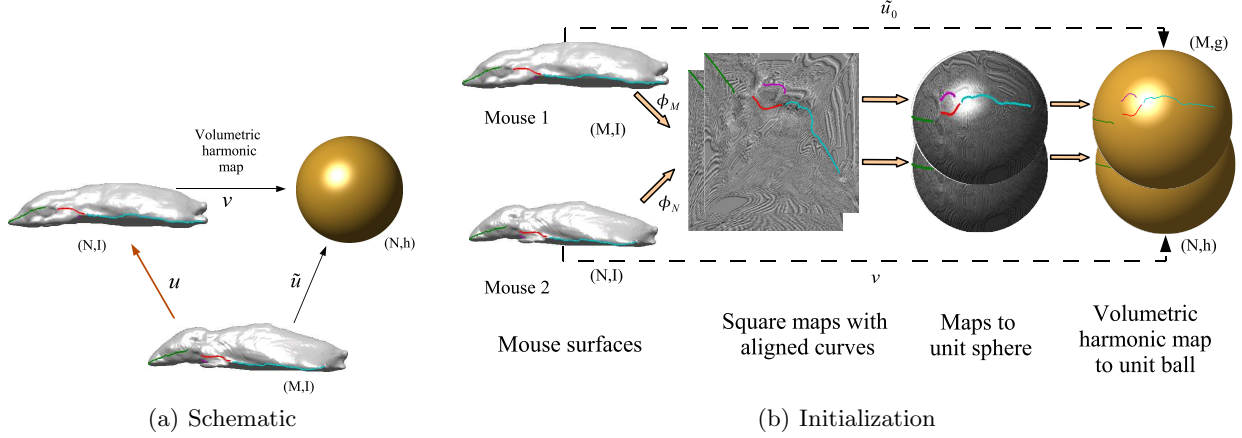
**Figure 1.** (a) Illustration of our general framework for surface-constrained volume registration. We first compute the map $v$ from manifold $(N, I)$ to the unit ball to form manifold $(N, h)$. We then compute a map $\tilde{u}$ from $(M, I)$ to $(N, h)$. The final harmonic map from $(M, I)$ to $(N, I)$ is then given by $u = v^{-1} \circ \tilde{u}$. (b) The initialization for the mapping procedure. First we generate flat square maps of the two mice. Each mouse is bisected along a midsagital plane and each half mapped to a unit square. We then map the squares corresponding to each half of the mouse to a unit disk and project the disks onto the unit sphere. We then generate a volumetric map from each mouse to the unit ball. Since all these maps are bijective, the resulting map gives us a bijective point correspondence between the two mice. However, this correspondence is not optimal with respect to the harmonic energy of maps from the first mouse to the second, but is used as an initialization for minimization of (2)

special case when $(M, g)$ and $(N, h)$ are 3D Euclidean manifolds, $h_{\alpha\beta} = \delta_\alpha^\beta$, $g_{ij} = g^{ij} = \delta_i^j$, the Kronecker delta, or identity tensor, for $\alpha, \beta, i, j \in 1, 2, 3$, and the mapping energy simplifies to

$$E(u) = \int_M |\nabla u|^2 dV \tag{3}$$

where $\nabla$ is the usual gradient operator in $3D$ Euclidean space and $dV$ is the volume integral.[26] In order to map the mouse volume $M$ to the unit ball, we minimize this energy subject to the constraint that the surface of $M$ maps to the surface of the unit ball using the point-to-point correspondence defined by the flat mapping obtained. This problem is solved using numerical integration over the voxel lattice and finite differences to approximate the gradients in (3). We minimize the resulting function using conjugate gradients.

### 2.2.2. Harmonic Mapping Between the Two Mouse Volumes

The aforementioned procedure is applied to both mouse volumes $M$ and $N$ to generate maps to the unit ball $B(0, 1)$ (Figure 1). The mapping of the Euclidean coordinates in $M$ to the unit ball provides the initial estimate $\tilde{u}_0$ of the harmonic map $\tilde{u}$. We then refine this map by minimizing the harmonic energy in (2) from $(M, I)$ to $(N, h)$, the unit ball representation of $N$. Again, the problem is solved using numerical integration and finite difference operators, in this case accounting for the metric $h$ when computing these derivatives. In this mapping, the location of the landmark curves in $M$ are constrained using their initial mappings $\tilde{u}_0$ computed when flattening and matching the surfaces. Other points within the mouse are allowed to move freely to minimize the harmonic energy, subject to the constraint that all points on the surface map to $\|\tilde{u}\|^2 = 1$, which is achieved by adding a penalty function to the discretized form of (2).

The harmonic mapping procedure is implemented in the following steps:

1. Align the surfaces of both the mice $M$ and $N$.

2. Map the unit squares to unit disks by the transformation $(x, y) \rightarrow (\frac{x}{\sqrt{x^2+y^2}}, \frac{y}{\sqrt{x^2+y^2}})$ and then project them onto two hemispheres using $(x, y) \rightarrow (x, y, \pm\sqrt{x^2 + y^2})$.

3. Using this mapping of the surface to the unit sphere as the boundary condition, generate a volumetric harmonic map of $M$ and $N$ to the unit ball $B(0,1)$ as described previously.

4. Compute the metric $h$ associated with the unit ball $B(0,1)$ coordinates of $N$.

5. Minimize (2) holding the matched landmarks fixed, and letting the surface $\partial M$ slide along the unit spherical boundary of the unit ball.

6. Compute the deformation vector field $u(x) - x$ where $u = v^{-1} \circ \tilde{u}$ and apply this to map mouse volume $M$ to mouse volume $N$.

## 3. FORMULATION OF THE MULTISPECTRAL OBT FORWARD MODEL

In order to solve the inverse problem in OBT for the bioluminescent source distribution ($\mathbf{q}$), one has to solve the forward problem first. The forward problem is to predict the photon fluence ($\mathbf{b}$) on the boundary $\partial\Omega$ of the animal volume $\Omega$, given the distribution of the bioluminescent source ($\mathbf{q}$) and the tissue optical properties. The reduced scattering coefficient $\mu'_s(\mathbf{r}, \lambda)$, the absorption coefficient $\mu_a(\mathbf{r}, \lambda)$, and the refractive index $\eta(\mathbf{r}, \lambda)$ are all functions of the 3D location $\mathbf{r}$ in tissue, and of wavelength $\lambda$. In the near-infrared (NIR) region of the electromagnetic spectrum, the reduced scattering coefficient is much larger than the absorption coefficient, and as a consequence, the diffusion approximation to the radiative transport equation is used.[27] The diffusion equation for the animal geometry is solved by tessellating the volume, assigning optical properties based on the warping results to the tessellation elements and using a finite element method (FEM).[28] If we assume $n$ possible source locations inside the animal and $m$ detector locations on the surface then the measured data $\mathbf{b}(\lambda)$ can be modeled as:

$$\mathbf{b}(\lambda) = \mathbf{A}(\lambda)\mathbf{q} \tag{4}$$

where $\mathbf{A}(\lambda) \in \mathbb{R}^{m \times n}$ is the monochromatic forward model at wavelength $\lambda$ and $\mathbf{q} \in \mathbb{R}^n$ is the source distribution. Assume that optical data are collected in $h$ spectral bins over the wavelength range of interest. The multispectral forward model $\mathbf{A}_{mult}$ is formed by concatenating the individual weighted monochromatic forward models for each wavelength.[3] The measurements $\mathbf{b}_{mult}$ are concatenated similarly to obtain a system of the form

$$\mathbf{b}_{mult} = \mathbf{A}_{mult}\mathbf{q} \tag{5}$$

where

$$\mathbf{b}_{mult} = \left[ \begin{array}{cccc} \mathbf{b}^T(\lambda_1) & \mathbf{b}^T(\lambda_2) & \cdots & \mathbf{b}^T(\lambda_h) \end{array} \right]^T, \mathbf{b}_{mult} \in \mathbb{R}^{hm}$$

and

$$\mathbf{A}_{mult} = \left[ \begin{array}{cccc} s(\lambda_1)\mathbf{A}^T(\lambda_1) & s(\lambda_2)\mathbf{A}^T(\lambda_2) & \cdots & s(\lambda_h)\mathbf{A}^T(\lambda_h) \end{array} \right]^T, \mathbf{A}_{mult} \in \mathbb{R}^{hm \times n}.$$

Here $\mathbf{s} = \left[ \begin{array}{cccc} s(\lambda_1) & s(\lambda_2) & \ldots & s(\lambda_h) \end{array} \right]^T, \mathbf{s} \in \mathbb{R}^h$ represents the emission spectrum of the bioluminescent source for $h$ wavelength bins. Eq. 5 can be solved using the regularized pseudo-inverse method.

## 4. RESULTS AND DISCUSSION

### 4.1. Validation of Surface Based Registration

By applying the harmonic warping scheme, we can map a labeled atlas to any subject in a one-to-one manner. This allows us to estimate the internal anatomy of the subject from the labeled anatomy of the atlas mouse. Although estimation of anatomy based only on the surface information is inevitably inaccurate, it can align major anatomical features approximately and thus help in estimation of organ locations. This can lead to a a more accurate forward model and can potentially help in improving accuracy of the source reconstruction. To validate this claim, we adopted the following methodology. As an atlas we have a manually labeled mouse volume and the corresponding CT data.[1] We obtained a CT scan of a second mouse (the 'subject') and used the Automated Image Registration (AIR)[29,30] software with a 5th order polynomial warping to carry out an intensity based registration of the subject image volume and the atlas image volume. Organ labels from the atlas were then transferred to the subject using the deformation vector field computed by AIR. We call these the 'true labels' for the subject.

|         |         |                |
|---------|---------|----------------|
| (a) Atlas | (b) Subject | (c) Harmonically Mapped Atlas |
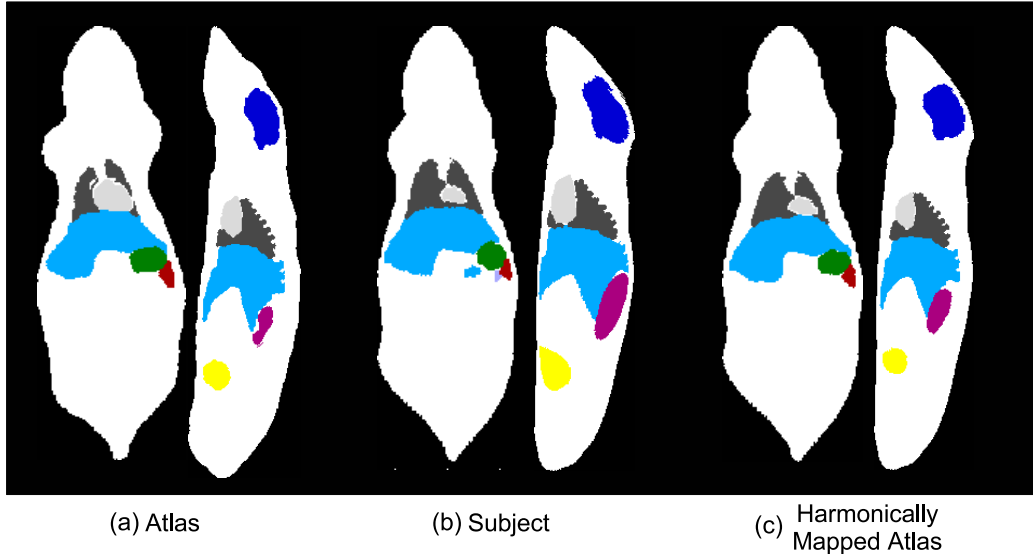
**Figure 2.** Example of surface constrained harmonic mapping. (a) Labeled atlas volume; (b) labeled subject volume; (c) registration of atlas to subject using surface constrained harmonic mapping. Note that the surface matches that of the subject.

**Table 1.** Comparison of Dice coefficients

| Organs | Rigid Registration | Harmonic Mapping |
|--------|--------------------|------------------|
| Brain | 0.6612 | 0.7047 |
| Liver | 0.6194 | 0.6508 |
| Kidney | 0.3779 | 0.4363 |
| Lungs | 0.3695 | 0.4871 |
| Heart | 0.4610 | 0.4673 |
| Bladder | 0.3839 | 0.3632 |
| Skeleton | 0.1339 | 0.1572 |
| Stomach | 0.4488 | 0.4957 |
| Spleen | 0.1862 | 0.2208 |
| Pancreas | 0.1410 | 0.1736 |
| Mouse Interior | 0.6599 | 0.8241 |

A triangulated surface representation of the subject mouse was obtained using the BrainSuite software.[31] The surface consisted of 397,767 triangles. 4 constraint curves delineating the limbs of the animal were marked on the mouse and atlas surfaces using the curve tracing module of BrainSuite. A harmonic map from the atlas to the subject was then computed using only surface information. The organ labels from the atlas were then transferred to the subject using the computed harmonic map. We denote these as the 'estimated labels' for the subject.

The accuracy of registration was quantified as the overlap between 'true' and 'estimated' labels using Dice coefficients. The Dice coefficient measures the intersection of any two sets $S_1$ and $S_2$ and is defined as $\frac{2|S_1 \cap S_2|}{|S_1| + |S_2|}$ where $|\cdot|$ denotes size of the set or equivalently the number of voxels in each labelled organ.[21] A comparison of the Dice coefficients for our harmonic mapping method and for rigid registration, again using surface information only, is shown in Table 4.1. The table indicates clear improvements in alignment of structures using our harmonic method when compared to the rigid registration approach. While the rigid registration does not accurately match the two surfaces, the harmonic mapping does. However, even when the surfaces are aligned, the corresponding deformation of the interior volume is ambiguous so that our regularized harmonic mapping has limited accuracy.

## 4.2. OBT Forward Model and Reconstruction

The volume of the subject was tessellated into 471,974 tetrahedrons and 79,670 nodes using the delaunay tetrahedralization method. Tissue labels from the warped atlas were transferred to the corresponding tetrahedrons in the space of the subject and optical properties were assigned element-wise to 11 tissue types (brain, liver, kidneys, lungs, heart, muscle, bladder, skeleton, stomach, spleen, and pancreas) based on published results.[2] 7,530 sources were defined inside the animal volume with a grid spacing of 1.6 mm and multispectral data were simulated at 2,530 surface nodes. The bioluminescent source is assumed to have the emission spectrum of firefly luciferase.[32] The multispectral optical forward model for the warped atlas ($\mathbf{W}$) was assembled for six 20 nm-wide wavelength bands between 560 nm and 660 nm using an efficient finite-element solver. The forward model ($\mathbf{H}$) corresponding to the homogeneous mouse volume was generated by assigning muscle optical properties to all internal organs. To evaluate the accuracy of the two forward models, a 'true' model ($\mathbf{T}$) was computed. This was done using the internal organ structure for the subject. We present correlation results between $\mathbf{T}$ and $\mathbf{W}$, and between $\mathbf{T}$ and $\mathbf{H}$ for representative sources located in 5 internal organs (kidneys, stomach, lungs, heart and the brain). Further, we analyze localization errors for the representative sources when $\mathbf{W}$ or $\mathbf{H}$ are used for inversion instead of $\mathbf{T}$. The inversion in all cases was carried out using an $L_2$ regularized pseudo-inverse.[33]

## 4.3. Correlation Analysis of Optical Forward Fields

In order to evaluate the accuracy of the forward solution, we computed the correlation coefficients between the true model $\mathbf{T}$ and the warped atlas $\mathbf{W}$, and those between the $\mathbf{T}$ and the homogeneous animal volume forward model $\mathbf{H}$. The correlation coefficients between $\mathbf{T}$ and $\mathbf{W}$ were computed for all source locations for every surface node. The average of these coefficients was R = 0.98 as against that between $\mathbf{T}$ and $\mathbf{H}$ which was R = 0.95. We also compared the models by computing correlations across the set of surface nodes for representative source locations. Table 4.3 shows the organs in which the sources were located and the corresponding average correlation coefficients. Both the detector and source correlation studies indicate that the forward model computed from warped labels $\mathbf{W}$ is closer to the true forward model $\mathbf{T}$ than the homogeneous mouse forward model $\mathbf{H}$ and provides a better approximation. Consequently, we expect improved reconstruction results when solving the OBT inverse problem using $\mathbf{W}$ in place of the homogeneous model $\mathbf{H}$.

**Table 2.** Correlation coefficients computed for representative sources in internal organs across all surface nodes

| Organ | # of sources | Warped | Homogeneous |
|-------|-------------|--------|-------------|
| Kidney | 841 | 0.98 | 0.96 |
| Stomach | 437 | 0.93 | 0.95 |
| Lungs | 1044 | 0.98 | 0.93 |
| Heart | 565 | 0.99 | 0.96 |
| Brain | 1008 | 0.94 | 0.94 |

## 4.4. Localization Accuracy using the Warped and Homogeneous OBT Forward Models

In the absence of noise, the regularized pseudo-inverse gives accurate reconstruction results if the true forward model is used for data generation and source reconstruction and the regularization parameter $\alpha$ is small. If the model is anatomically perturbed, as is the case here when using the warped atlas or the homogeneous model, this solution becomes distorted and a larger $\alpha$ value needs to be chosen. As the regularization parameter is increased, the resolution drops and, for sufficiently large $\alpha$, reconstructed distributions tend to be superficial. For the studies presented here we empirically selected an optimal value for $\alpha$ to approximately optimize performance for both $\mathbf{H}$ and $\mathbf{W}$ keeping a fixed value for all studies. Table 4.4 shows the percentage of sources accurately reconstructed using the true animal geometry to generate the data, and the warped and homogeneous forward models for inversion. We define the localization error as the spatial distance between the maxima of the smoothed reconstructed solution and the true source location. These results indicate a higher percentage of sources are accurately reconstructed using the warped model $\mathbf{W}$ although the differences are smaller than we might have expected based on the earlier comparison of Dice coefficients.

**Table 3.** Table shows the percentage of sources that were accurately reconstructed within 1.6 mm (one grid spacing) of the original source location.

| Organ | Kidney | Stomach | Lungs | Heart | Brain |
|---|---|---|---|---|---|
| # of sources | 841 | 437 | 1044 | 565 | 1008 |
| Warped | 76 | 58 | 81 | 87 | 54 |
| Homogeneous | 71 | 57 | 71 | 85 | 53 |

Figure 4.4 shows a simulation study conducted for a tumor located deep in the mouse. The reconstructed distribution using the homogeneous mouse forward model tends to be deeper in tissue than the true location. This can be attributed to the variation in optical properties for different tissue types in that region. Reconstruction results using the warped model show more accurate localization in this case. These results indicate that in some cases it may be advantageous to use the warped atlas rather than a homogeneous model although the results shown in Table 4.4 indicate that the fraction of sources where localization is substantially improved may be relatively small.



(a)                               (b)                               (c)
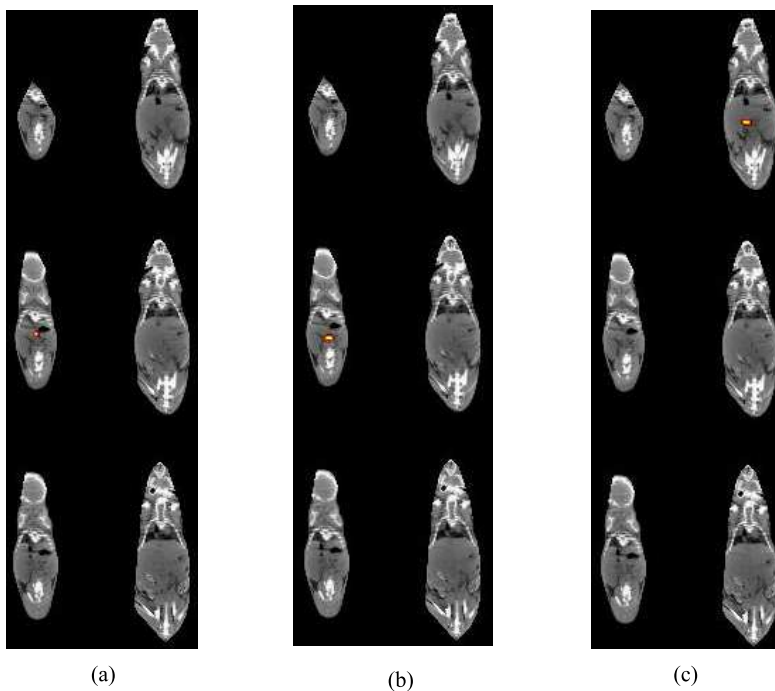
**Figure 3.** OBT reconstructions for a tumor located deep in the mouse: (a) shows the original source location, (b) shows the 3D reconstructed distribution using the warped model and (c) shows the reconstructed distribution for the source using the homogeneous model

## 5. CONCLUSION

We have developed a novel volumetric warping scheme with surface and landmark constraints and applied it to atlas-based bioluminescent source reconstruction in OBT. Analysis of correlation coefficients between the data from the warped, homogeneous and the true models showed warping by the method presented here yielded a more accurate photon transport model than the one obtained by assuming the mouse to be homogeneous. Simulation results of localization error show small but consistent improvements in localization accuracy compared to the homogeneous model. Consequently in general use we might expect this approach to lead to some improvement in overall accuracy of the reconstructed images, although clearly, direct access to anatomical images of each subject

would result in further improvements. A potentially more powerful application of this approach is in longitudinal studies in which functional images are acquired over time but only a single anatomical image is acquired. The warping procedure described here could be used to realign this anatomical image each to each of the functional studies using surfaces obtained with structured light methods.

# REFERENCES

1. B. Dogdas, D. Stout, A. F. Chatziioannou, and R. M. Leahy, "Digimouse: a 3D whole body mouse atlas from CT and cryosection data," *Physics in Medicine and Biology* **52**(3), pp. 577–587, 2007.
2. G. Alexandrakis, F. R. Rannou, and A. F. Chatziioannou, "Tomographic bioluminescence imaging by use of a combined optical-pet (opet) system: a computer simulation feasibility study," *Physics in Medicine and Biology* **50**(17), pp. 4225–4241, 2005.
3. A. J. Chaudhari, F. Darvas, J. R. Bading, R. A. Moats, P. S. Conti, D. J. Smith, S. R. Cherry, and R. M. Leahy, "Hyperspectral and multispectral bioluminescence optical tomography for small animal imaging," *Physics in Medicine and Biology* **50**, pp. 5421–5441, Nov 2005.
4. G. Alexandrakis, F. R. Rannou, and A. F. Chatziioannou, "Effect of optical property estimation accuracy on tomographic bioluminescence imaging: simulation of a combined optical-PET (OPET) system," *Physics in Medicine and Biology* **51**(8), pp. 2045–2053, 2006.
5. G. Wang, E. A. Hoffman, G. McLennan, L. V. Wang, M. Suter, and J. F. Meinel, "Development of the first bioluminescence CT scanner," *Radiology* **299**(P), 2003.
6. B. W. Rice, O. Coquoz, C. Kuo, N. Nantel, D. N. Nilson, D. G. Strearns, T. L. Troy, D. Zwarg, and M. D. Cable, "Advances in 2D in vivo optical imaging instrumentation," *Abstracts of the 2nd Annual Meeting of the Society for Molecular Imaging (San Francisco, CA)* , 2003.
7. G. Wang, W. Cong, K. Durairaj, X. Qian, H. Shen, P. Sinn, E. Hoffman, G. McLennan, and M. Henry, "In vivo mouse studies with bioluminescence tomography," *Optics Express* **14**, pp. 7801–7809, 2006.
8. C. A. Pelizzari, G. T. Y. Chen, D. R. Spelbring, R. R. Weichselbaum, and C. T. Chen, "Accurate three-dimensional registration of ct, pet and/or mr images of the brain," *J. Comput. Assist. Tomogr.* **13**(1), pp. 22–26.
9. P. Thompson and A. Toga, "A surface-based technique for warping 3-dimensional brain," *IEEE Transactions on Medical Imaging* **15**(4), pp. 1–16, 1996.
10. N. Krahnstover and C. Lorenz, "Development of point-based shape representation of arbitrary three-dimensional medical objects suitable for statistical shape modeling," **3661**, pp. 620–631.
11. J. H. Downs, J. L. Lancaster, and P. T. Fox, "Surface based spatial normalization using convex hulls," in *Brain Warping*, Academic, (San Diego, CA), 1999.
12. T. Hartkens, D. Hill, A. D. Castellano-Smith, D. Hawkes, C. Maurer, A. Martin, W. Hall, and C. T. H. Liu, "Using points and surfaces to improve voxel-based non-rigid registration," **2**, pp. 565–572, (Tokyo), Sept 2002.
13. C. Davatzikos, J. Prince, and R. Bryan, "Image registration based on boundary mapping," *IEEE Transactions on Medical Imaging* , 1996.
14. C. Davatzikos and J. Prince, "Brain image registration based on curve mapping," pp. 245–254, 1994.
15. S. C. Joshi and M. I. Miller, "Landmark matching via large deformation diffeomorphisms," *IEEE Transactions on Image Processing* **9**, August 2000.
16. G. Gerig, S. Joshi, T. Fletcher, K. Gorczowski, S. Xu, S. M. Pizer, and M. Styner, "Statistics of population of images and its embedded objects: Driving applications in neuroimaging," in *ISBI*, pp. 1120–1123, April 2006.
17. J. Glaunés, M. Vaillant, and M. I. Miller, "Landmark matching via large deformation diffeomorphisms on the sphere," *J. Math. Imaging Vis.* **20**(1-2), pp. 179–200, 2004.
18. T. Liu, D. Shen, and C. Davatzikos, "Deformable registration of cortical structures via hybrid volumetric and surface warping," *NeuroImage* **22**(4), pp. 1790–1801, 2004.
19. W. Han, W. Cong, and G. Wang, "Mathematical study and numerical simulation of multispectral bioluminescence tomography," *International Journal of Biomedical Imaging* **2006**, 2006.
20. C. Studholme, D. L. G. Hill, and D. J. Hawkes, "An overlap invariant entropy measure of 3d medical image alignment," *Pattern Recognition* **32**(1), pp. 71–86, 1999.

21. A. P. Zijdenbos, B. M. Dawant, R. A. Margolin, and A. Palmer, "Morphometric analysis of white matter lesions in mr images," *IEEE Transactions on Medical Imaging* **13**, pp. 716–724, Dec. 1994.

22. A. A. Joshi, D. W. Shattuck, P. M. Thompson, and R. M. Leahy, "A framework for registration, statistical characterization and classification of cortically constrained functional imaging data," in *Lecture Notes in Computer Science*, **3565**, pp. 186–196, July 2005.

23. S. Nishikawa, *Variational Problems in Geometry*, vol. 205 of *Translations of Mathematical Monographs*, AMS, 2001.

24. B. Tang, G. Sapiro, and V. Caselles, "Diffusion of general data on non-flat manifolds via harmonic maps theory: The direction diffusion case.," *International Journal of Computer Vision* **36**(2), pp. 149–161, 2000.

25. F. Mémoli, G. Sapiro, and S. Osher, "Solving variational problems and partial differential equations mapping into general target manifolds," *J. Comput. Phys.* **195**(1), pp. 263–292, 2004.

26. Y. Wang, X. Gu, and S. T. Yau, "Volumetric harmonic map," *Communications in Information and Systems* **3**(3), pp. 191–202, 2004.

27. S. Arridge, "Optical tomography in medical imaging," *Inverse Problems* **15**(2), pp. 41–93, 1999.

28. S. R. Arridge, M. Schweiger, M. Hiroaka, and D. T. Delpy, "A finite element approach for modeling photon transport in tissue," *Phys. Med. Biol.* **20**(2), pp. 299–309, 1993.

29. R. P. Woods, S. T. Grafton, C. J. Holmes, S. R. Cherry, and J. C. Mazziotta, "Automated image registration: I. General methods and intrasubject, intramodality validation," *Journal of Computer Assisted Tomography* **22**, pp. 139–152, 1998.

30. R. P. Woods, S. T. Grafton, J. D. G. Watson, N. L. Sicotte, and J. C. Mazziotta, "Automated image registration: II. Intersubject validation of linear and nonlinear models," *Journal of Computer Assisted Tomography* **22**, pp. 153–165, 1998.

31. D. W. Shattuck and R. M. Leahy, "BrainSuite: An automated cortical surface identification tool.," in *MICCAI*, S. L. Delp, A. M. DiGioia, and B. Jaramaz, eds., *Lecture Notes in Computer Science* **1935**, pp. 50–61, Springer, 2000.

32. B. W. Rice, M. D. Cable, and M. B. Nelson, "In vivo imaging of light-emitting probes," *Journal of Biomedical Optics* **6**(4), pp. 432–440, 2001.

33. G. H. Golub and C. F. Van Loan, *Matrix Computations*, The John Hopkins University Press, MD, 3 ed., 1996.